Chapter 9
Functionally Graded Metallic Biomaterials

Yoshimi Watanabe, Hisashi Sato, and Eri Miura-Fujiwara

Abstract In functionally graded materials (FGMs), the composition and/or microstructure gradually changes over the volume [3–5], resulting in corresponding changes in the properties of the materials. There are many areas of application for FGMs, and one of them is biomedical application. In this chapter, at first, the merits of the metallic biomaterials with graded composition and/or microstructure are described. Then, microstructures and mechanical properties of Ti/biodegradable-polymer FGMs for bone tissue by spark plasma sintering (SPS) method, continuous graded composition in Ti–ZrO_2 bio-FGMs by mixed-powder pouring method, and Al-based FGMs containing TiO_2 nanoparticles with antibacterial activity by a centrifugal mixed-powder method are introduced. Also, our experimental results of white ceramic coating on Ti–29Nb–13Ta–4.6Zr alloy for dental application and magnetic graded materials by inhomogeneous heat treatment of SUS304 stainless steel are given.

Keywords Functionally graded materials (FGMs) • Metal matrix composite (MMC) • Centrifugal force • Spark plasma sintering (SPS) • Ti–29Nb–13Ta–4.6Zr alloy • Photocatalyst • Stainless steel

9.1 Functionally Graded Materials (FGMs) for Biomedical Applications

Biomaterials should simultaneously satisfy many requirements and possess properties such as nontoxicity, corrosion resistance, thermal conductivity, strength, fatigue durability, biocompatibility, and sometimes esthetics [1]. A single composition with a uniform structure may not satisfy all such requirements. For example, in the case of a dental implantation, the part positioned inside the jaw bone needs more biocompatibility and affinity for bone formation, while the other part

Y. Watanabe (✉) • H. Sato
Nagoya Institute of Technology, Gokiso-cho, Showa-ku, Nagoya 466-8555, Japan
e-mail: yoshimi@nitech.ac.jp

E. Miura-Fujiwara
University of Hyogo, Himeji, Japan

M. Niinomi et al. (eds.), *Advances in Metallic Biomaterials*, Springer Series in Biomaterials Science and Engineering 4, DOI 10.1007/978-3-662-46842-5_9

positioned outside jaw bone and exposed to intraoral conditions needs the mechanical properties and good fit of shape to adapt to prosthetic appliances [2]. However, although the surface is sometimes modified with a coating layer, currently used implants have mostly uniform composition and structure inside each material layer. To satisfy such requirements and possess properties within one material simultaneously, the concept of functionally graded materials (FGMs) is very useful, where FGMs are the advanced composite materials characterized by spatial variations in composition and/or microstructure that changes over the volume [3–5]. Figure 9.1 illustrates the compositional and functional differences between coated-type or joined-type composite and FGMs. The coated-type or joined-type composite, shown in Fig. 9.1a, is a type of macroscopically inhomogeneous material with *material A* at one end and *material B* at the other. The most serious problem with the coated-type or joined-type composite is a macroscopic interface. Since the functions of this material change discretely from the *material A* part to the *material B* part at the macroscopic interface, cracking and/or delamination should occur near/at the interface during processing or use of the part. This problem can be overcome by eliminating the macroscopic interface, as shown in Fig. 9.1b, where the composition and/or microstructure varies gradually. Thus, the properties should be changed continuously by the absence of a macroscopic interface in the FGMs.

The suitable properties for dental implant are shown in Fig. 9.2. For the case of uniform implant, the properties such as strength and biocompatibility are constant throughout the implant material. On the other hand, the implant with compositional gradient could control the functions of mechanical properties and biocompatibility, depending on the necessity of each part of implant, without the abrupt change due to the formation of discrete boundary [6]. Thus, the so-called trade-off relation can be overcome by the idea of FGMs.

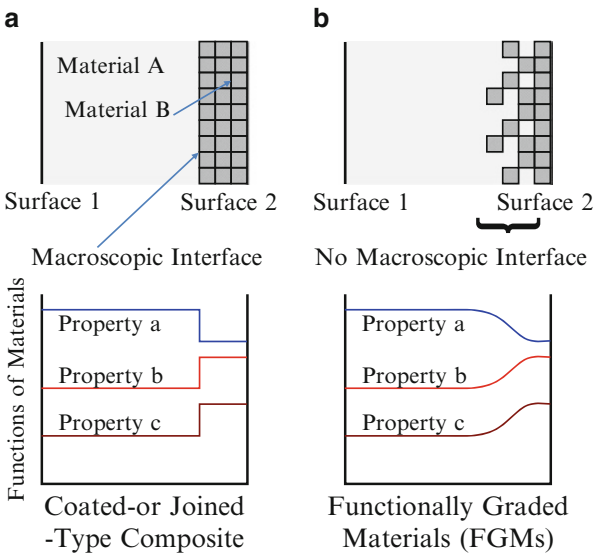

Fig. 9.1 The compositional and functional differences between coated-type or joined-type composite and FGMs

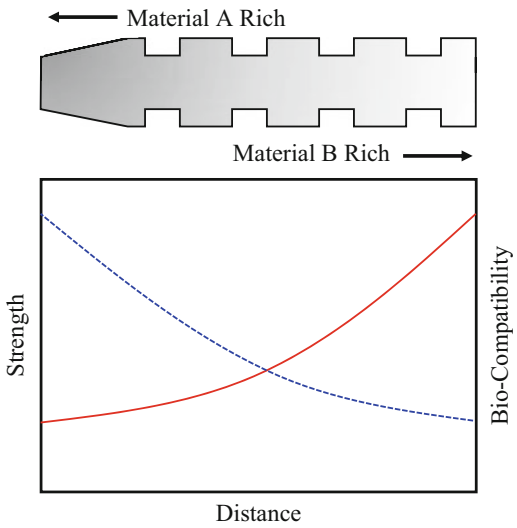

Fig. 9.2 Suitable properties of functionally graded dental implant

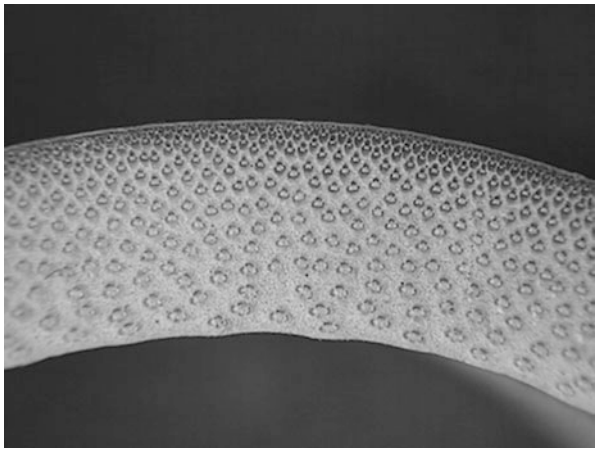

Fig. 9.3 Transversal cross section of bamboo stem

Indeed, we can find many FGMs structures in nature; this is because biological systems such as plant stems and tree stems, animal bones, mollusk shells, and other biological hard tissues tend to be optimized for the loading conditions, to which they are subjected [5]. Human tissues have been also developed and remodeled in such a way to best adapt the function requirements. Consequently, the biological systems are complicated and non-uniform. For example, bamboo and certain other plants have excellent characters based on functionally graded structures [7]. Figure 9.3 shows a cross section of bamboo stem. The matrix of bamboo is filled by soft tissue cells called parenchymatous cells, and that is longitudinally reinforced by strong fibers called the vascular bundle sheath. Graded structure of

the density, size, and shape of the vascular bundle sheath can be found along the radial direction.

A number of FGMs fabrication methods have been proposed and comprehensive reports have been given on the general fabrication methods [3–5]. In general, there are three approaches to fabricate FGMs, as shown in Fig. 9.4. The first one is to eliminate the interface of coated-type or joined-type composite, eliminating discontinuities in the properties at the interface, as shown in Fig. 9.4a. Compositional gradient can be formed by elimination of the sharp interface by diffusion. The second one is to induce non-uniform distributions of dispersoids in a homogeneous particle composite, creating multiple functions within the material, as shown in Fig. 9.4b. One example is centrifugal method. In the centrifugal method, a centrifugal force applied to a homogeneous molten composite assists the formation of the desired gradation. The composition gradient is then achieved primarily due to the difference in the centrifugal force produced by the difference in density between the molten metal and solid particles [8]. The apparatus for the centrifugal method and motion of solid particles under the centrifugal force are shown in Fig. 9.5. The third one is carried out by sequential buildup of layers, as shown in Fig. 9.4c. Powder processing, thermal spray processing, chemical vapor deposition (CVD), and physical vapor deposition (PVD) are the typical examples.

Fabrication of FGMs by the powder processing is schematically illustrated in Fig. 9.6. At first, *material A* and *material B* are weighed and mixed. Then, graded compacts are produced by sequentially layering the powder mixture in the die according to a predesigned spatial distribution of the composition. Finally, the sintering is carried out by hot isostatic pressing (HIP), pressureless sintering after cold isostatic pressing (CIP) compaction, hot press, and spark plasma sintering (SPS).

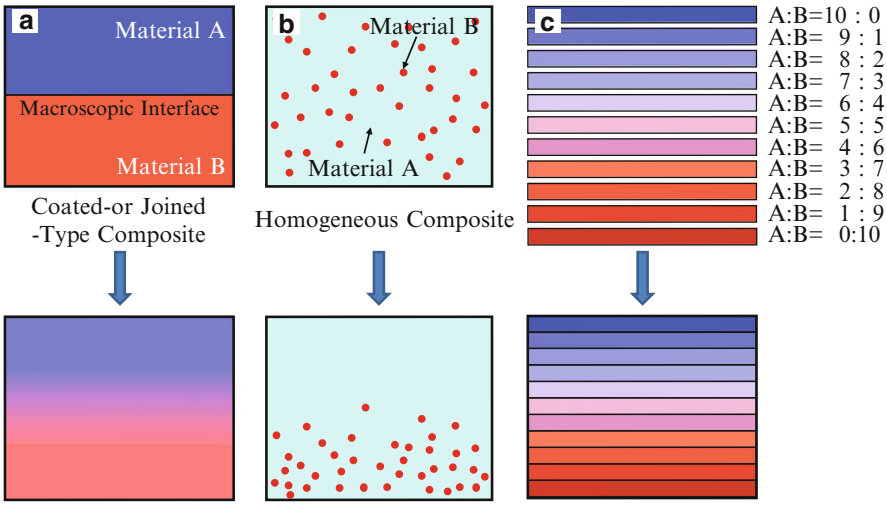

Fig. 9.4 Three approaches to fabricate FGMs

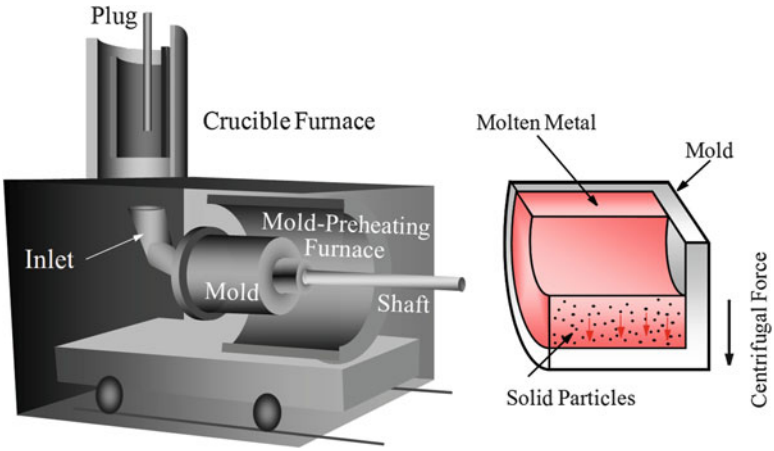

Fig. 9.5 The apparatus for the centrifugal method and motion of solid particles under the centrifugal force

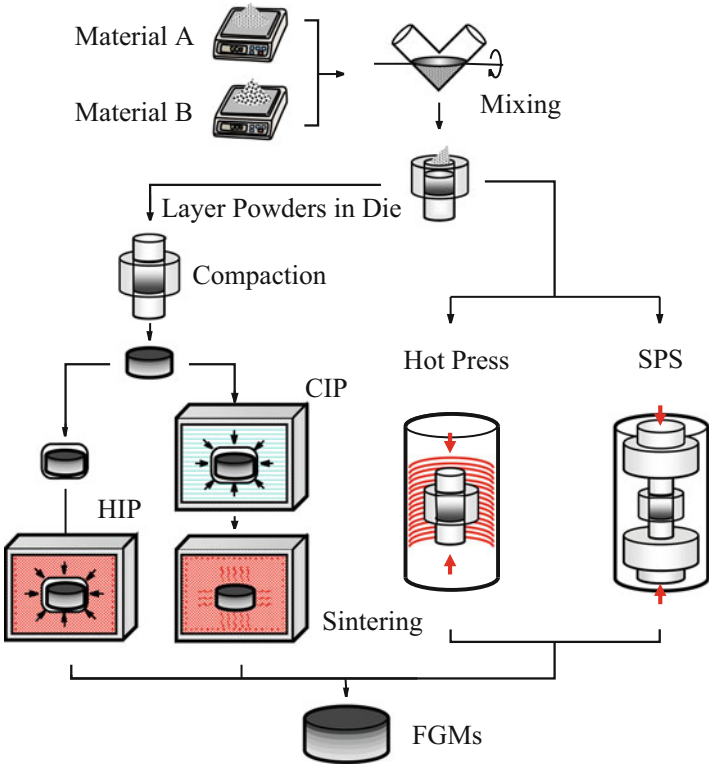

Fig. 9.6 Fabrication process of the FGMs by powder processing

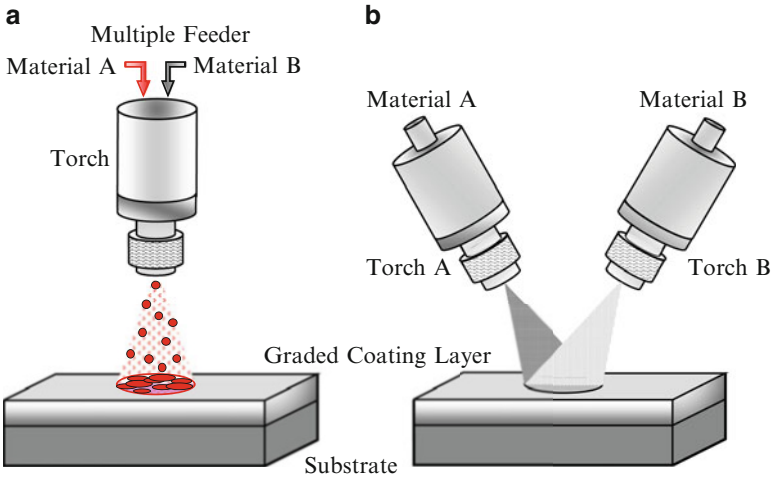

Fig. 9.7 Fabrication of the FGMs by thermal spray processing. (**a**) Multiple feeder method and (**b**) multiple torch method

In thermal spraying, feedstock material (coating precursor) is introduced into a combustion or plasma flame. The molten or semimolten micrometer-sized particles are accelerated toward substrates, and coatings are made by the accumulation of numerous sprayed particles. Since the deposit by the thermal spray processing is formed through the sequential buildup of layers, a number of approaches can be used to produce a graded deposit [9]. Figure 9.7a, b shows multiple feeder method and multiple torch method, respectively. In the case of multiple feeder method, *material A* and *material B* are simultaneously introduced into the plasma jet by changing the mixture ratio. On the other hand, in the case of multiple torch method, *material A* and *material B* are deposited through torch A and torch B, respectively, with optimum spray parameters for each material.

Functionally graded biomaterials are also fabricated by several methods. For example, titanium nitride–apatite functionally graded implants are fabricated by SPS method [10]. It is reported that functionally graded Ti–HAP coatings on Ti–6Al–4V have been fabricated by chemical solution deposition [11]. Ti–TiC–C gradient biomaterial has been prepared by means of plasma source ion implant–ion beam enhanced deposition [12]. Functionally graded (Ca–Ti–O)-(Ca–P–O) bioceramic film is formed by metal organic chemical vapor deposition (MOCVD) method [13]. In this chapter, our recent experimental results, Ti/biodegradable-polymer FGMs for bone tissue fabricated by SPS method, continuous graded composition in Ti–ZrO_2 bio-FGMs fabricated by mixed-powder pouring method, white ceramic coating on Ti–29Nb–13Ta–4.6Zr alloy for dental application, Al-based FGMs containing TiO_2 nanoparticles with antibacterial activity by a centrifugal mixed-powder method, and magnetic graded materials by inhomogeneous heat treatment of SUS304 stainless steel will be introduced.

9.2 Ti/Biodegradable-Polymer FGMs for Bone Tissue Fabricated by SPS Method [14]

Ti and Ti alloys are widely used as metallic implants due to their excellent mechanical properties, corrosion resistance, and nontoxic behavior. However, the Young's modulus of currently used Ti alloys (90–110 GPa) is still not ideal compared with that of human bone (10–20 GPa), which may lead to premature failure of the implant [15, 16]. Therefore, the low Young's modulus Ti alloys are required to decrease the stress-shielding effect in bone implant coupling, enhancing bone regeneration and avoiding resorption process. In order to reduce the apparent elastic modulus of Ti and its alloys, recently, porous Ti and its alloys have been developing. Moreover although they are classified into bioinert materials, a conduction of living bone occurs on the surface of implanted materials that reside in the body for a long period. This can lead to refracture of cured bone in removal operations [17].

Meanwhile, poly-L-lactic acid (PLLA) has attracted much attention, because it is biodegradable, compostable, producible from renewable resources, and nontoxic to the human body and the environment [18]. If Ti-based biocomposites containing PLLA could be fabricated, the PLLA can be gradually decomposed inside the body with progress of time, and then the pore can be generated into the Ti matrix during repairing of the bone. Since the bone can simultaneously penetrate into the pore, the Ti matrix can be tightly bonded with the bone. However, there is a large difference of melting point between Ti and PLLA. Namely, the melting points of Ti and PLLA are 1,670 °C and around 170–180 °C, respectively. Therefore, the process of the Ti-based biocomposite containing PLLA must be done at relative lower temperature; as a result, the strength of the obtained composite becomes lower [19]. Alternatively, the space holder method is applied. Porosity is generated by removing the spacer that was sintered with the base material [20, 21]. Moreover, for the bulk mechanical property, fabricated Ti–PLLA composite must have lower Young's modulus, while wear resistance around the surface must be improved. Such trade-off relation can be overcome by the concept of FGMs.

Prior to fabricating the Ti–PLLA FGMs, the Ti–NaCl composite was fabricated by SPS method using powder mixture of commercially pure (CP) Ti powder (under 56 μm) and NaCl (hexahedron shapes; some of the NaCl particle size was over 500 μm) to complete the sintering of Ti matrix, since the difference in melting points of these materials is relatively small. Volume fractions of NaCl powder were 30 vol%, 50 vol.%, and 70 vol.%. The Ti–NaCl powder mixture was sintered at 700 °C for 5 min under applied stress of 30 MPa. Figure 9.8a, b shows optical microscope (OM) images of Ti–30vol.%NaCl and Ti–70vol.%NaCl composites, respectively [14]. The upper and lower pictures were observed on plane Z_0 and plane R, respectively. As can be seen in Fig. 9.8, oblate NaCl particles are observed on the plane R, whereas there is no anisotropic microstructure on the plane Z_0. That is, NaCl particles are compressed during the SPS process.

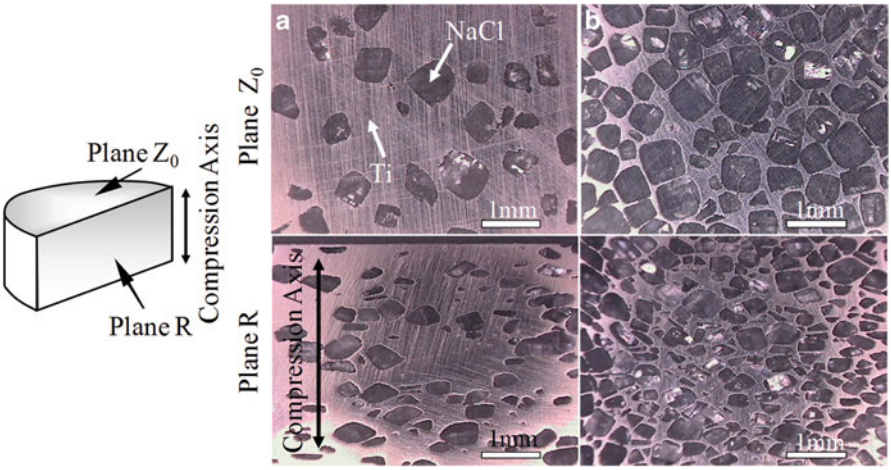

Fig. 9.8 OM images of (**a**) Ti–30 vol.%NaCl and (**b**) Ti–70 vol.%NaCl composites at plane Z_0 and plane R before dissolving NaCl particles (Reprinted from Ref. [14], Copyright 2011, with permission from Elsevier)

The Ti–NaCl composites were put into hot water of 100 °C to obtain porous Ti. Hereafter porous Ti samples obtained from Ti–30vol.%NaCl, Ti–50vol.%NaCl, and Ti–70vol.%NaCl composites by the dissolution process are abbreviated to porous Ti(30), porous Ti(50), and porous Ti(70), respectively. It is found that porous Ti(50) and porous Ti(70) samples have no remained NaCl particles, and porous Ti(50) and porous Ti(70) have open pores. Figure 9.9 shows the pore size distribution in the porous Ti(50) [14]. In these graphs, mean pore size range in the specimen distributes within 200–600 μm. It is reported that the optimal pore size in porous bone substitutes to obtain differentiation and growth of osteoblasts and vascularization is approximately 300–400 μm or 200–500 μm [22]. Thus, the obtained porous Ti is satisfied the basic requirement of biomedical pores of hard tissues.

Relationship between bulk density and porosity was investigated as shown in Fig. 9.10 [14]. As can be seen, the more porosity increased, the more density decreased linearly. Since the density of bone is 1.6–2.0 Mg/m^3, the porous Ti(50) has closed value to the range of bone density. In addition, at least the most of all pores is supposed to be open pore and no residual NaCl remained in the bulk in Ti (50).

Young's modulus and 0.2 % proof stress of pure Ti and porous Ti samples are shown in Fig. 9.11a, b, respectively [14]. Young's modulus and 0.2 % proof stress of samples are decreased with increasing volume fraction of pores (porosity). Moreover, anisotropy of these properties is found for porous Ti samples. Although Young's modulus of pure Ti is close to the required one, 0.2 % proof stress of pure Ti is much larger than the required yield stress. On the other hand, Young's modulus of the porous Ti(30) is smaller than the required modulus, and its 0.2 %

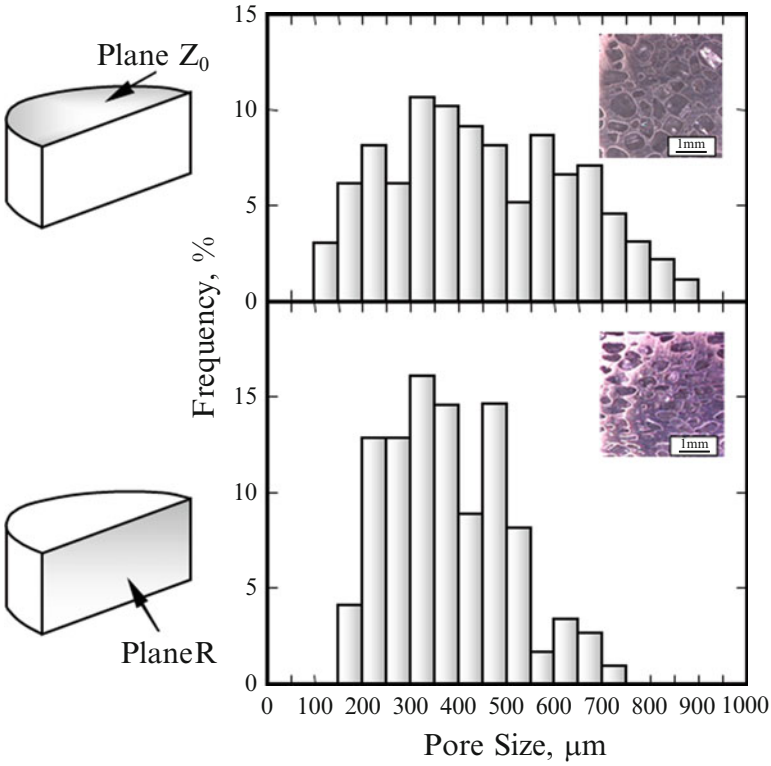

Fig. 9.9 The pore size distributions in the porous Ti(50) at plane Z_0 and plane R (Reprinted from Ref. [14], Copyright 2011, with permission from Elsevier)

Fig. 9.10 Relationship between bulk density and porosity in porous Ti (Reprinted from Ref. [14], Copyright 2011, with permission from Elsevier)

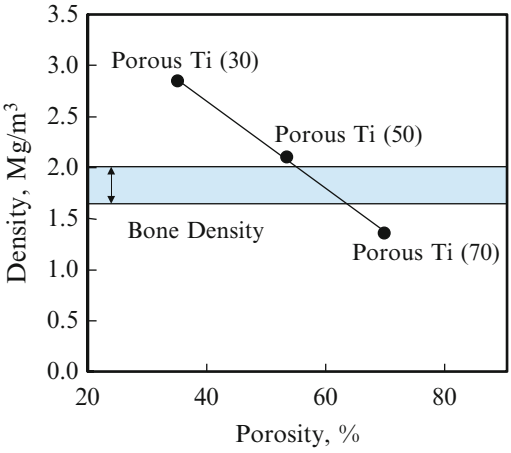

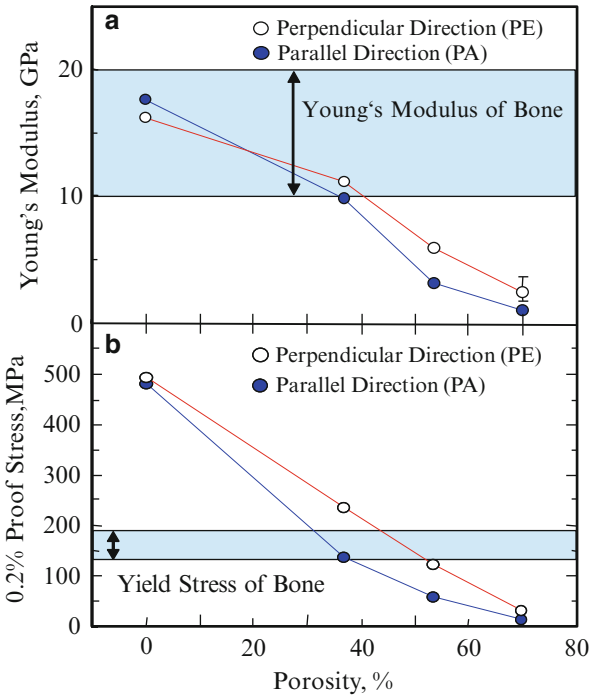

Fig. 9.11 Young's modulus and 0.2 % proof stress of pure Ti and porous Ti samples. Compression axes are along perpendicular (PE) and parallel (PA) direction (Reprinted from Ref. [14], Copyright 2011, with permission from Elsevier)

proof stress is almost the same stress with ideal metallic implant material. From these results, it is found that porous Ti(30) can satisfy both requirements of Young's modulus and yield stress as a metallic implant material by means of improving its Young's modulus, although the porous Ti(30) does not have open pores. In addition, porous Ti(50) has open pores and it is likely to be able to satisfy the requirements by means of adding a reinforcement material into pores. Biodegradable material such as PLLA would be one of expectable materials as reinforcement filler.

To fabricate the Ti–PLLA FGMs, porous Ti sample obtained from Ti–NaCl composites with 50 vol.% NaCl and PLLA pellets were mixed in recovery flask, and the flask was heated at about 200 °C to melt PLLA pellets. After porous Ti samples were covered with melted PLLA, an aspirator vacuumed the samples in the flask to remove the air in pores. Following the procedures, the flask was reverted to atmospheric pressure and then melting PLLA was introduced into the pores of porous Ti samples. Figure 9.12a, b shows OM micrographs showing the Ti–PLLA FGMs sample fabricated from porous Ti(50) at surface region (Plane Z_0) and interior region (Plane $Z_{h/3}$), respectively [14]. It seems that PLLA is successfully introduced into the Ti matrix. It must be noted here that some pores are observed on the Plane $Z_{h/3}$ as shown in Fig. 9.12b, while there is no pore on Plane Z_0 as shown in Fig. 9.12a. The amount of pore changes from place to place, and such porosity

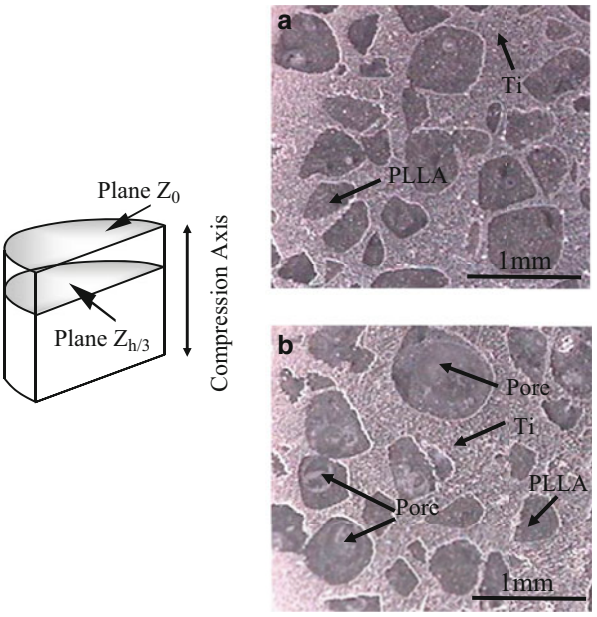

Fig. 9.12 OM images at (**a**) plane Z_0 and (**b**) plane $Z_{h/3}$ in Ti–PLLA FGMs sample fabricated from porous Ti (50) (Reprinted from Ref. [14], Copyright 2011, with permission from Elsevier)

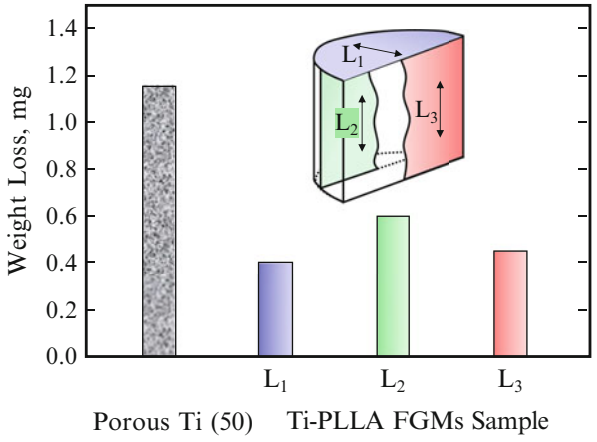

Fig. 9.13 Results of wear tests sliding along three different directions under reciprocal movement (Reprinted from Ref. [14], Copyright 2011, with permission from Elsevier)

distribution could cause gradients of mechanical properties in the fabricated Ti–PLLA FGMs sample.

Wear tests for fabricated Ti–PLLA FGMs sample were performed using a ball-on-disk-type machine, where the samples were slid along three different directions under reciprocal movement against a stationary counter sphere of stainless steel. The results are shown in Fig. 9.13, as well as that from porous Ti(50) [14]. It is seen that osmotic PLLA into porous Ti enhances its wear resistance. Since PLLA is much softer than Ti matrix, it is supposed that PLLA near worn surface was

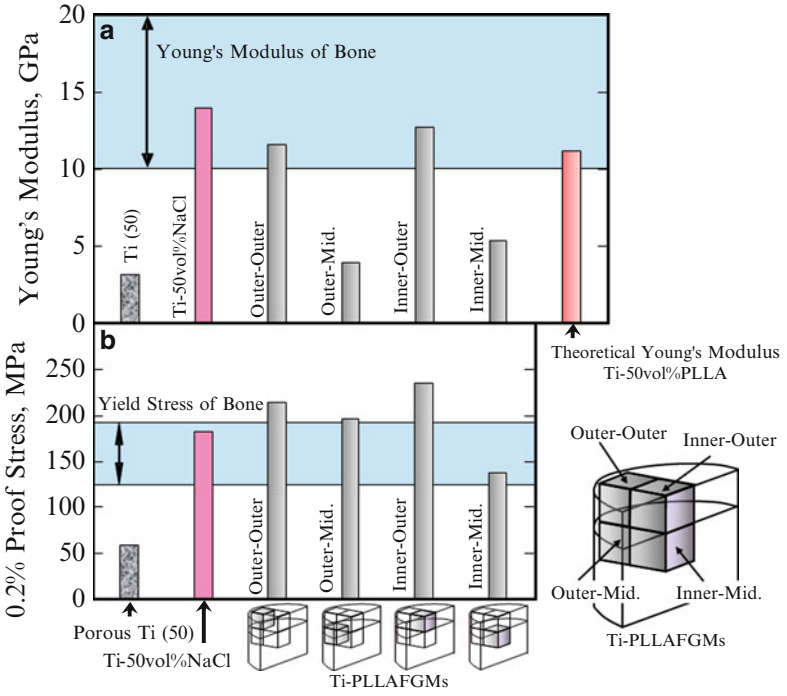

Fig. 9.14 (**a**) Young's modulus and (**b**) 0.2 % proof stress of porous Ti(50), Ti–50 vol.%NaCl composite and Ti–PLLA FGMs with different regions. Theoretical Young's modulus of Ti–50 vol.%PLLA FGMs is also shown in (**a**) (Reprinted from Ref. [14], Copyright 2011, with permission from Elsevier)

preferentially scraped out from the Ti–PLLA FGMs sample and subsequently spreads out and covers on the Ti matrix during friction. It is considered that preferential abrasion and coating of PLLA due to wear protects against wear of Ti matrix and reduces adhesion of counter-face with Ti.

Young's modulus and 0.2 % proof stress of porous Ti, Ti–NaCl composite, and Ti–PLLA FGMs sample with different parts are shown in Fig. 9.14a, b, respectively. As shown in Fig. 9.14a, the porous Ti(50) has the lowest Young's modulus, since it has a porous structure. On the contrary, the highest Young's modulus was observed for the pore-free Ti–NaCl composite, which is within the range of the modulus of the bone. Theoretical Young's modulus of Ti–PLLA FGMs calculated by simple rule of mixture is also shown in this figure. It should be noted that the Young's modulus values of Ti–PLLA FGMs samples from outer–outer and inner–outer positions were in excellent agreement with the theoretical one. 0.2 % proof stress of Ti–PLLA FGMs also changes from place to place. In this way, the mechanical property gradients are observed for Ti–PLLA FGMs, which may be caused by the volume fractional gradient of pores, as shown in Fig. 9.12. Since Young's modulus and 0.2 % proof stress of the Ti–PLLA FGMs sample are close to

the required ones, Ti–PLLA FGMs satisfy the required mechanical properties of metallic implant material by means of PLLA dispersion in porous Ti. It can be expected that optimum performance will be obtained just after implantation of the composite into the bone, and then PLLA will gradually degrade and be absorbed into the body. Although its mechanical properties will become lower as PLLA degrades, osteogenesis will occur in the pore instead.

9.3 Continuous Graded Composition in Ti–ZrO_2 Bio-FGMs Fabricated by Mixed-Powder Pouring Method

In session 9.1, it is described that the powder processing has many advantages to fabricate the FGMs. However, the graded structure fabricated by the powder processing becomes stepwise structure, and it is, unfortunately, difficult to produce the FGMs with continuous gradients. By a centrifugal slurry method, this shortcoming can be overcome. For centrifugal slurry method, slurry with two types of solid particles will be used, namely, high-velocity particle with larger density and/or larger particle size and low-velocity particle with smaller density and/or smaller particle size, as shown in Fig. 9.15a [8, 23]. Since the motion of solid particles in viscous liquid under centrifugal force can be determined by the Stokes' law, the terminal velocity is reached at a very early stage of the centrifugal casting method [24, 25]. Therefore, the velocity of particles within a liquid under centrifugal force, dx/dt, can be expressed as

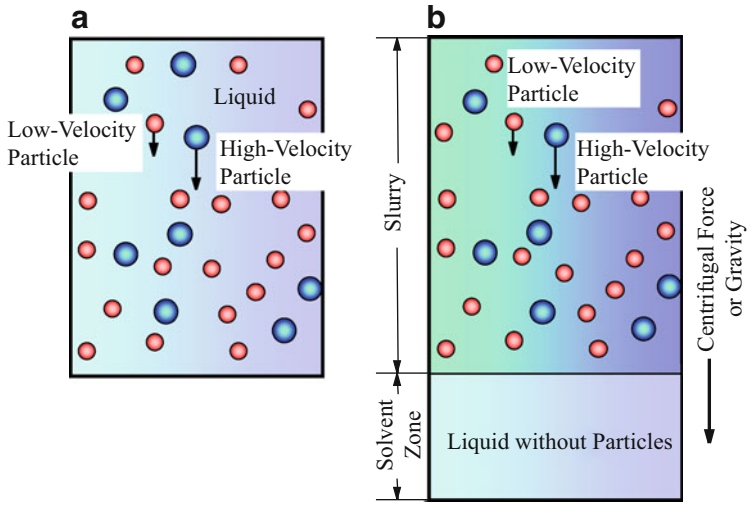

Fig. 9.15 Fabrication process to obtain green body with continuous gradient under a centrifugal force. (**a**) Centrifugal slurry method [8] and (**b**) centrifugal slurry-pouring method [27]

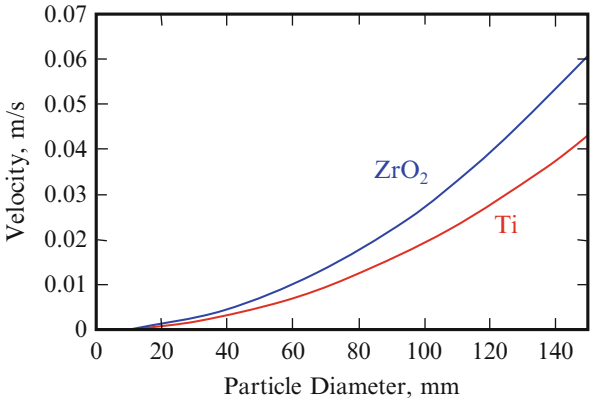

Fig. 9.16 Velocities of Ti and ZrO_2 particles under the centrifugal force [23]

$$\frac{dx}{dt} = \frac{|\rho_p - \rho_m| G g D_p^2}{18\eta} \tag{9.1}$$

where ρ_p, ρ_m, D_p, G, g, and η are density of particle, density of liquid, particle diameter, G number showing the level of centrifugal force, gravitational acceleration, and apparent viscosity of liquid, respectively. The continuous gradient can be obtained by the difference of migration rate between the two kinds of particles, i.e., high-velocity particle and low-velocity particle, predicted by Eq. 9.1. After complete sedimentation occurs, the liquid part of the slurry will be removed, and a green body with continuous gradient can be obtained. The green body is, then, subjected to sintering, and finally an FGMs sample with continuous gradient can be fabricated.

In order to verify and confirm the above idea, we shall focus on the Ti–ZrO_2 FGMs. ZrO_2 ceramics have several advantages over other ceramic materials, due to the transformation-toughening mechanisms operating in their microstructure that can give to components made out of them, very interesting mechanical properties [26]. Partially stabilized ZrO_2 (PSZ) and tetragonal ZrO_2 polycrystal (TZP) are common biomaterials used in orthopedic applications. Figure 9.16 shows migration velocities of Ti and ZrO_2 particles under the centrifugal force [8, 23], where the densities of Ti and ZrO_2 are 4.5 Mg/m^3 and 5.95 Mg/m^3, respectively. When the particle size is the same, the velocity of ZrO_2 particle is higher than that of Ti particle, due to its larger density. On the other hand, if the slurry contains the smaller ZrO_2 particles and larger Ti particles, the Ti particles can have high velocity in a specific condition.

Compositional gradient of the FGMs sample fabricated by the centrifugal slurry method is simulated for the Ti–ZrO_2 system with particle sizes of 63 ~ 90 μm for Ti particle and 75 ~ 106 μm for ZrO_2 particle. In this case, Ti particle becomes low-velocity particle and ZrO_2 particle becomes high-velocity particle. Results are shown in Fig. 9.17a [27]. In this figure, the horizontal axis is the normalized position of the green body, and 0.0 and 1.0 correspond to the top and bottom

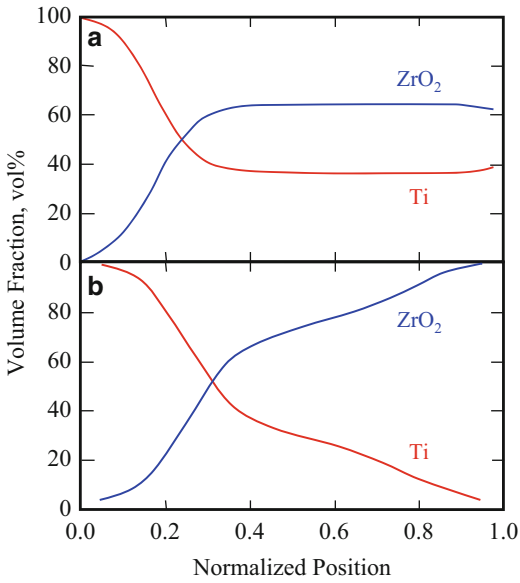

Fig. 9.17 Distributions of Ti and ZrO_2 particles within the FGMs fabricated by (**a**) the centrifugal slurry method and (**b**) the centrifugal slurry-pouring method (computer simulation) [27]. In (**b**), width of solvent zone is 100 mm

surfaces of the settled green body, respectively. This result clearly indicates that continuous gradient can be obtained by the centrifugal slurry method. However, large compositional gradient (from 0 vol.% at one end to 100 vol.% at another end of the FGMs sample for specific component) cannot be achieved, since the low-velocity Ti particles placed at the bottom region before the sedimentation still may remain around the same region after the complete sedimentation.

To solve the above shortcoming, a slurry-pouring method has been proposed to fabricate the FGMs with large compositional gradient [8, 23]. The slurry with high-velocity particle and low-velocity particle was poured into the spinning mold with solvent zone, as shown in Fig. 9.15b. The existence of solvent zone increases the sedimentation period. As a result, large compositional gradient, for example, from 0 vol.% at one end to 100 vol.% at another end, can be fabricated. The computer simulation is conducted for the slurry-pouring method, and results are shown in Fig. 9.17b; here the width of solvent zone is 100 mm [8, 23]. It must be noted here that the FGMs sample has a continuous gradient, and the volume fraction of Ti at the normalized position of 0.0 is 0 vol.%, while 100 vol.% at 1.0 position. Thus, a large compositional gradient can be achieved by the slurry-pouring method.

An experimental study of the slurry-pouring method was conducted where crushed ice is used as the particle suspension medium to control the particle sediment from the initiation to the end [28]. The hollow tube was filled with the crushed ice of 78.5×10^{-6} m^3, prepared using the ice crusher, as shown in Fig. 9.18a [28]. A hollow tube with a length of 220 mm made of plastic was fitted and sealed to another end of the graphite die. The height of the total suspension, i.e., the length of the hollow tube along with the graphite die is 250 mm. Homogeneously mixed powders of Ti and ZrO_2 with a volume ratio 1:1 were poured from

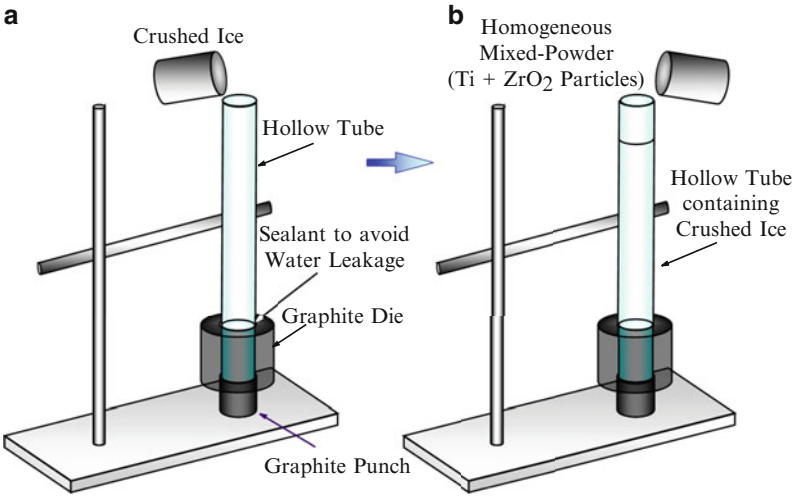

Fig. 9.18 Experimental setup of the slurry-pouring method. (**a**) Pouring crushed ice into a hollow tube and (**b**) pouring homogeneous Ti–ZrO_2 mixed powder into a hollow tube containing crushed ice [28]

the top of the crushed ice, as shown in Fig. 9.18b [28]. The crushed ice was allowed to melt gradually under isothermal conditions at 40 °C. Sedimentation of Ti and ZrO_2 particles proceeded along longitudinal direction of the hollow tube at the uniform temperature. The homogeneously mixed powders poured on the top of crushed ice will move down to the bottom of the graphite die. Sedimentation of the mixed powders depends on the densities and/or sizes of the particles. After settlement, a green body with compositional gradient was obtained.

The concentrations of Ti and ZrO_2 at each region were analyzed by energy-dispersive X-ray spectrometry (EDX), and the volume fraction distributions of Ti and ZrO_2 in FGMs were obtained as shown in Fig. 9.19 [28]. The particle size ranges of Ti particle and ZrO_2 particle are 63–90 μm and 75–106 μm for Fig. 9.19a, 45 μm pass and 38–75 μm for Fig. 9.19b, and 90–150 μm and 106–150 μm for Fig. 9.19c, respectively. The results of computer simulation are also shown in these figures [28]. It can be seen from these figures that the volume fraction of Ti is close to 100 vol.% between the normalized positions of 0 and 0.2 in all the samples. The composition of Ti decreases and that of ZrO_2 increases continuously and gradually, to become nearly homogeneous between normalized positions of 0.6 and 0.65. The volume fraction of ZrO_2 reaches close to 100 vol.% between the normalized positions 0.8 and 1, as shown in Fig. 9.19a, b. Therefore, it is found that the proposed method is an effective fabrication technique for FGMs with large and continuous compositional gradient. The hardness values in Ti–ZrO_2 FGMs samples are also shown in these figures. The hardness inside the fabricated FGMs increases

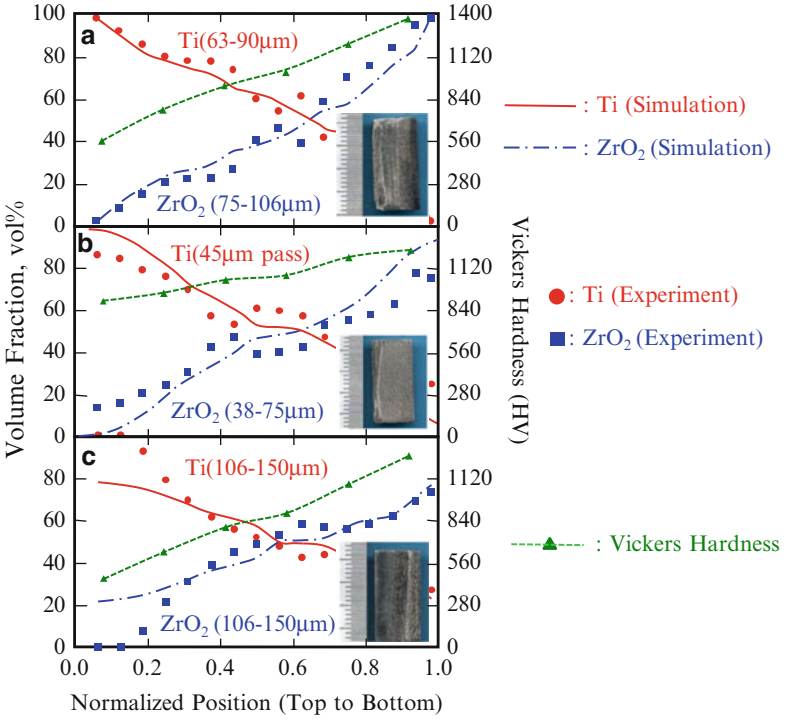

Fig. 9.19 Comparison of experimental volume fraction results with simulation results and effects of hardness number in Ti–ZrO_2 FGMs fabricated from different particle sizes [28]

with the increase in normalized position 0–1, thereby confirming the increasing ZrO_2 content across the normalized position. In this way, bio-FGMs with hardness gradient can be obtained.

9.4 White Ceramic Coating on Ti–29Nb–13Ta–4.6Zr Alloy for Dental Application

Although ceramic materials are becoming popular and starting to substitute for metallic parts of dental devices, such as dental implant, crown, denture, bracket, wire, and so on, metals are superior to in terms of ductility. Presently, a ceramic fused metallic core crown is commonly used, not only by the biological and mechanical requirements but also the esthetic requirement. However, exfoliation between metallic core and ceramic surface is one of the most serious clinical problems [29]. If one can obtain white-colored metallic materials, which own high ductility, high strength, and excellent esthetic properties, this problem is overcome. Not only Pt group or Au group alloys but also Ti alloys have been

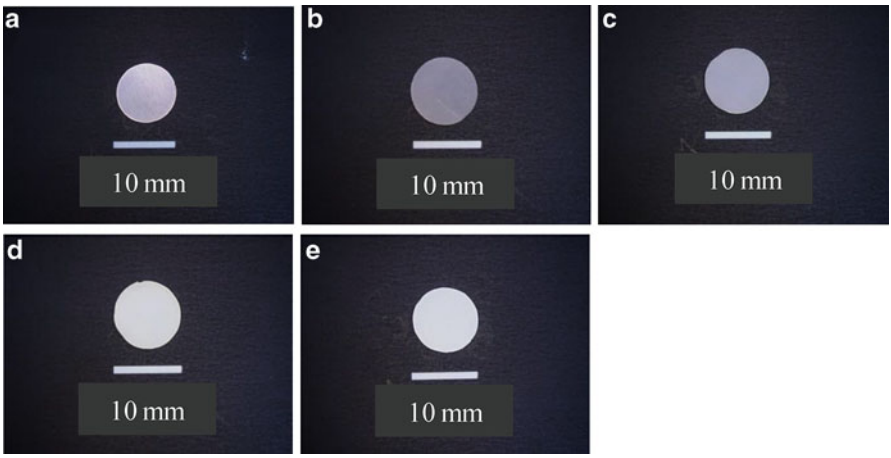

Fig. 9.20 Appearances of TNTZ sample surfaces. (**a**) Before oxidation treatment. (**b**) Oxidation treated at 900 °C for 1.8 ks, (**c**) at 900 °C for 3.6 ks, (**d**) at 1,000 °C for 1.8 ks, and (**e**) at 1,000 °C for 3.6 ks [34]

used for dental materials because of their high corrosion resistance and excellent mechanical properties. Since it is known that a white-colored TiO_2 layer is formed by high-temperature oxidation of pure Ti, it is expected that a white oxide film can be also formed by heat treatment on Ti alloys. Ti–29Nb–13Ta–4.6Zr (TNTZ) alloy is a β-type Ti alloy with excellent mechanical properties as a biomedical load-bearing material developed by Niinomi et al. [30, 31]. The ideal metallic white materials could be realized when esthetically and mechanically excellent oxide coating having durability against exfoliation of TNTZ can be made. As described in session 9.1, compositional gradient can be formed by elimination of the sharp interface by diffusion. White ceramic coating on TNTZ and Ti with graded microstructure for dental applications is, thus, carried out by oxidation treatment [32–34].

Hot-rolled TNTZ and pure Ti bars with a diameter of ϕ10 mm were used as a substrate material. After annealing at 800 °C, the bar was sliced with a thickness of about 1 mm. The slices were polished with emery paper up to #1,500. The polished samples were oxidized in air furnace at 800 °C, 900 °C, 1,000 °C, and 1,200 °C from 0.6 ks to 10.8 ks. The samples were air-cooled after heat treatment. Macroscopic appearance of TNTZ sample before and after oxidation treatment is shown in Fig. 9.20 [34]. It is obvious that matte and bright oxide film was formed on the metallic TNTZ surface after oxidation. Brightness visually increased with increasing holding time or oxidized temperature; however, the oxidation film peeled off after long-time and/or high-temperature treatment. Although the figure is not presented here, the oxidation film of the TNTZ substrate oxidized at 1,000 °C for 7.2 ks exfoliated from the substrate completely after oxidation. This is because of the difference of thermal expansion between the oxide and metal substrate. To solve this problem, slow cooling and oxidation at minimum temperature were examined.

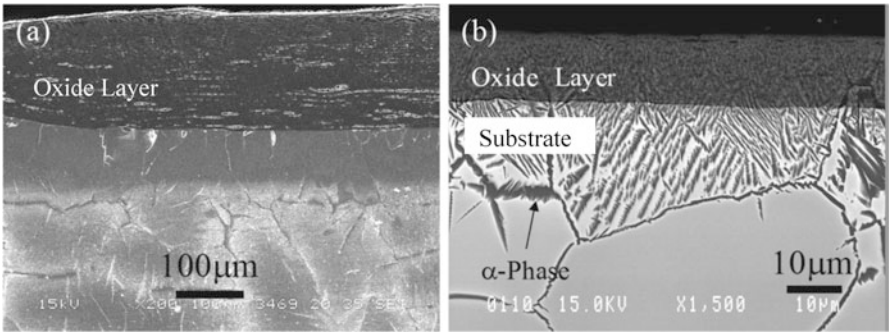

Fig. 9.21 SEM cross-sectional images around surface of oxidized (**a**) Ti and (**b**) TNTZ samples. The oxidation treatment was carried out at 1,000 °C for 3.6 ks and furnace cooling for Ti sample and 1,000 °C for 1.8 ks and air cooling for TNTZ sample (Reprinted from Ref. [33], with permission from TMS)

From our results, oxidation at 1,000 °C for 3.6 ks for Ti and 1,000 °C for 1.8 ks was the best heat treatment condition in terms of avoiding exfoliation during oxidation.

Cross-sectional microstructures of Ti and TNTZ after oxidation treatment were investigated by SEM, and results are shown in Fig. 9.21a, b, respectively [33]. In Fig. 9.21a, the oxide layer of Ti exhibited unique microstructure with a stratified formation, which means an oxide particle layer and a gap stacked one by one. On the other hand, dense oxide layer was formed on TNTZ substrate as shown in Fig. 9.21b. Regarding substrate microstructure in Fig. 9.21b, grain growth during oxidation was observed in substrate beneath the oxide layer; in addition, lamellar structure was observed in the grain of TNTZ. This lamellar structure consisted of the $\alpha + \beta$-phase. The α-phase was precipitated owing to O diffusion during oxidation since O acts as an α-phase stabilizer. The α-phase close to the interface contained about 20 mol% of O, whereas the matrix had less than 10 mol% of O. Concurrently, Nb and Ta concentrations at the α-phase were lower than in the matrix.

In order to obtain detailed information about oxide/substrate interface, depth profile of chemical composition was studied by X-ray photoelectron spectroscopy (XPS) for TNTZ sample oxidized at 1,000 °C for 1.8 ks. The obtained results are shown in Fig. 9.22 [32]. In this figure, it seems both O and Ti contents were homogeneous in the oxide layer, and O rapidly decreased at the lamellar structure layer. After that, O gradually decreased in substrate. On the other hand, Ti content was uniform in the substrate and decreased rapidly at the lamellar structure and then Ti content became uniform at the oxide layer. Content ratio Ti/O was close to 1:2; thus, TiO_2 was considered to be a major oxide. In addition, depth profile of other elements, Nb, Ta, and Zr, seemed to have a similar tendency to that of Ti. These elements are supposed to form oxide. According to XRD measurements, although which is not shown here, not only TiO_2 but also $Ti(Nb, Ta)_2O_7$ and/or $Ti(Nb, Ta)O_4$ were detected in the oxide layer.

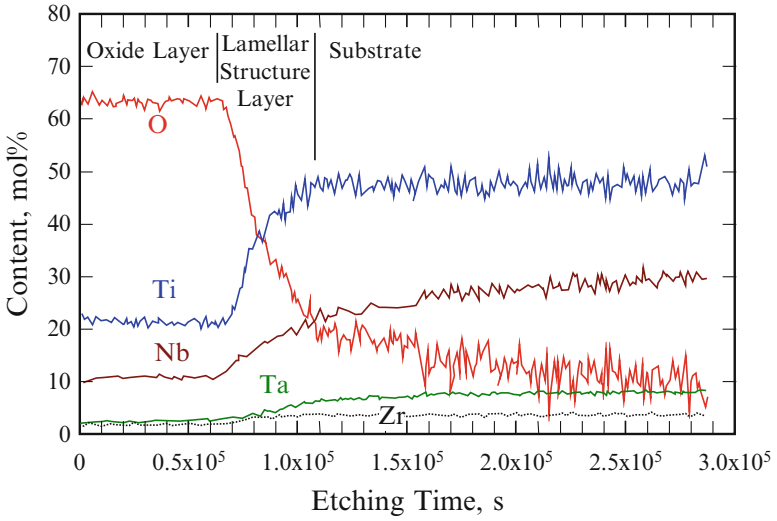

Fig. 9.22 XPS depth profile of TNTZ oxidized at 1,000 °C for 1.8 ks [32]

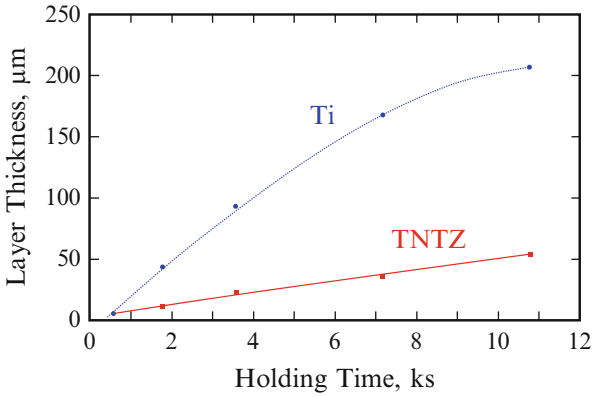

Fig. 9.23 Relationship between oxide layer thickness and holding time of TNTZ and Ti (Reprinted from Ref. [33], with permission from TMS)

Figure 9.23 shows the relationship between thickness of the oxide layer and holding time [33]. Thickness of the oxide layer was measured from a cross-sectional image taken by SEM. It is seen that thickness of the oxide layer increased with increasing holding time in both TNTZ and Ti samples. Moreover, the oxide layer thickness of Ti at each oxidation time in this figure is bulk thickness; thus, true oxide thickness should be thinner than the appearance.

The color of the oxidized surface was measured using a spectrophotometric colorimeter. Color was expressed in terms of L*a*b* color system (CIE1976) [35]. In this color system, color space was expressed by the parameter of brightness L* and chromaticity coordinates a* and b*. L* indicates brightness, and a* and b* express redness (+) ~ greenness (−) and blueness (+) ~ yellowness (−), respectively, as shown in Fig. 9.24.

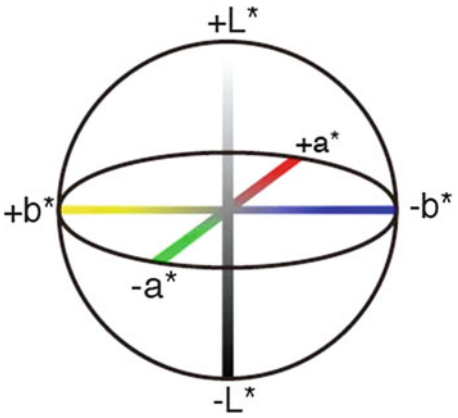

Fig. 9.24 L*a*b* color space in a 3-dimensional display showing CIELab color system [35]. Copyright (2014)The Japan Society of Applied Physics

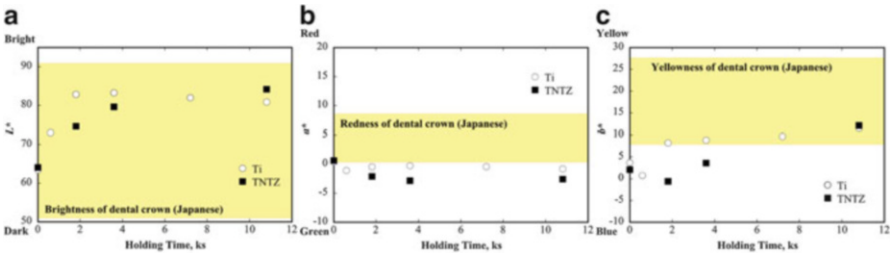

Fig. 9.25 Relationships between holding time and (**a**) L*, (**b**) a*, and (**c**) b* parameters (Reprinted from Ref. [33], with permission from TMS)

The color of the samples oxidized at 1,000 °C was measured using the spectrophotometric colorimeter. Figure 9.25 shows relationships between holding time and L*a*b* parameters. Color range of the crown of Japanese's natural tooth reported elsewhere [36] was also shown in these figures. In Fig. 9.25a, L* (bright–dark) of both Ti and TNTZ samples parabolically increased with increasing holding time at the initial stage of oxidation treatment, and then plateau appeared. Plateau region began from about 2 ks to 3.6 ks in Ti and TNTZ samples, respectively. It is noteworthy that L* of both Ti and TNTZ samples was in the range of Japanese's tooth color. Regarding b* (blue–yellow) shown in Fig. 9.25c, parabolic oxidation time dependence was observed as well as L*. It is considered from these results that L* and b* change depending on the thickness of the oxide layer. At short holding time, observed b* was out of the range in either Ti or TNTZ sample, and then b* also increased with increasing holding time. Thus, b* eventually reached within the range of tooth color. On the other hand, in Fig. 9.25b, a* (green–red) of both samples was below the range regardless of holding time, and time dependence on a* seemed to be negligible in the Ti sample and to be small but negative in the TNTZ sample. From these results, L* and b* increased with increasing holding time; thus, these parameters can be controlled by oxidation condition while exfoliation should

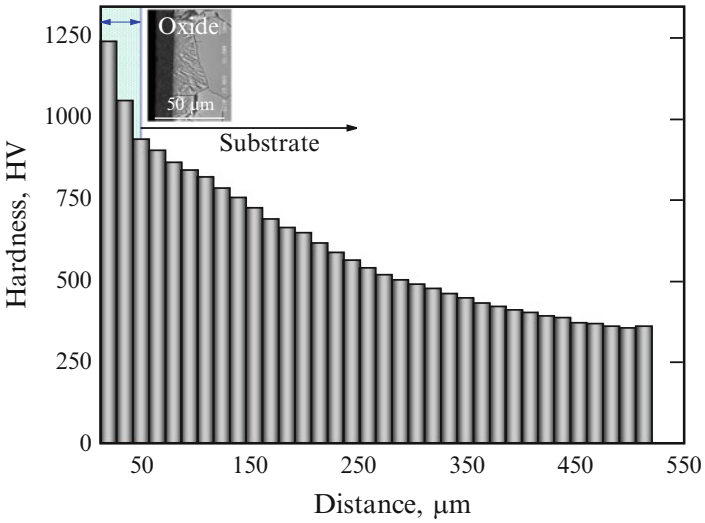

Fig. 9.26 Hardness distributions in oxidized TNTZ sample measured by nano-indentation hardness tester

be taken into account. It is reported that maximum brightness as an opaque resin for a facing metal crown is L* ≦ 80 [37]; therefore, brightness of the oxide film obtained in this study is sufficient for opaque material for artificial tooth.

Nano-indentation hardness tests of TNTZ sample were carried out and results are shown in Fig. 9.26. As can be seen, hardness of the oxide layer was higher than the substrate close to the oxide layer. Moreover, hardness is changed from place to place. This graded hardness in the oxide layer would come from microstructural difference inside the layer. However, details of microstructure inside the oxide layer are our future work. Formation of oxide layer with graded hardness may be one reason of the high exfoliation resistance of oxide/TNTZ.

9.5 Al-Based FGMs Containing TiO_2 Nanoparticles with Antibacterial Activity by a Centrifugal Mixed-Powder Method

Medical devices are highly susceptible to bacterial contamination. Various methods have been proposed to confer the biomaterials' antibacterial activity [38]. An anatase-type TiO_2 is well known as the most effective photocatalyst, and it shows useful self-cleaning, deodorizing, and antibacterial functions, even under weak UV light. For these applications, TiO_2 is prepared as nanosized crystals to bring out its full abilities [39]. With the above in mind, Al-based FGMs containing antibacterial TiO_2 particles have been developed. Since the photocatalytic and antibacterial TiO_2 particle has a nanosized diameter, the motion of TiO_2 particles with different

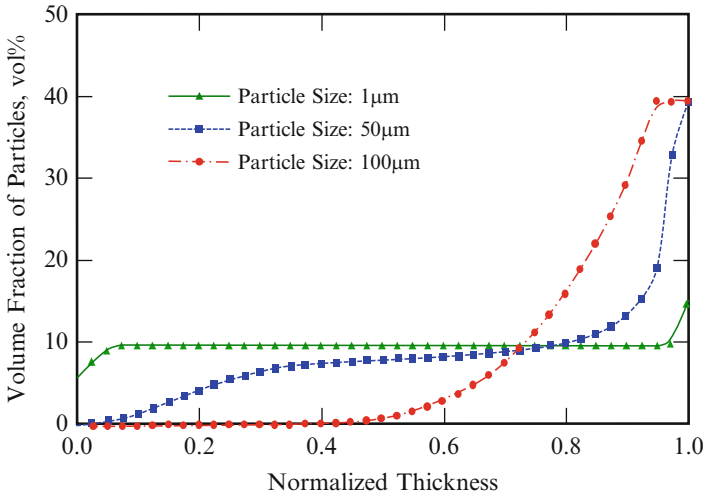

Fig. 9.27 Simulated particle distributions of TiO_2 in Al–TiO_2 FGMs fabricated by centrifugal method [40]

particle sizes in a molten Al under a centrifugal force is numerically modeled based on the Stokes' law (Eq. 9.1). Figure 9.27 shows the effect of particle size on the compositional gradient in the Al–TiO_2 FGMs fabricated by the centrifugal method shown in Fig. 9.5 [40]. These distributions of TiO_2 particles shown in Fig. 9.27 are obtained by calculation basing on Stokes' law. The volume fraction of TiO_2 and centrifugal force were fixed to be 10 vol.% and $G = 50$, respectively. The abscissa represents the position of normalized thickness of the ring, i.e., 0.0 is the inner surface and 1.0 is the outer surface. As can be seen, TiO_2 particles with 100 μm in diameter are gradually distributed in Al–TiO_2 FGMs sample; however, TiO_2 particles with 1 μm in diameter were almost homogeneously distributed in the sample. Therefore, it is concluded that the compositional gradient of nanoparticles in the FGMs fabricated by the centrifugal method is very small.

Alternatively, a centrifugal mixed-powder method is proposed as a novel processing technique to fabricate nanoparticle distributed FGMs. The experimental procedure of the centrifugal mixed-powder method is shown in Fig. 9.28 [40]. As a first step, a powder mixture of nanoparticles and metal matrix particles is inserted into a spinning mold, as shown in Fig. 9.28a. Then, molten metal matrix is poured into the spinning mold with the powder mixture, as shown in Fig. 9.28b. As a result, the molten metal matrix penetrates into the space between the particles due to the pressure exerted by the centrifugal force, as shown in Fig. 9.28c. At the same time, the metal matrix powder is melted by the heat from molten matrix poured from the crucible, as show in Fig. 9.28d. Finally, an FGMs ring with nanoparticles distributed on its surface can be obtained, as show in Fig. 9.28e. Using this processing method, Al–TiO_2 FGMs were fabricated.

Figure 9.29 shows the Ti concentration of Al–TiO_2 FGMs rings as a function of normalized thickness [40]. As can be seen, Ti concentration in both Al–TiO_2 FGMs

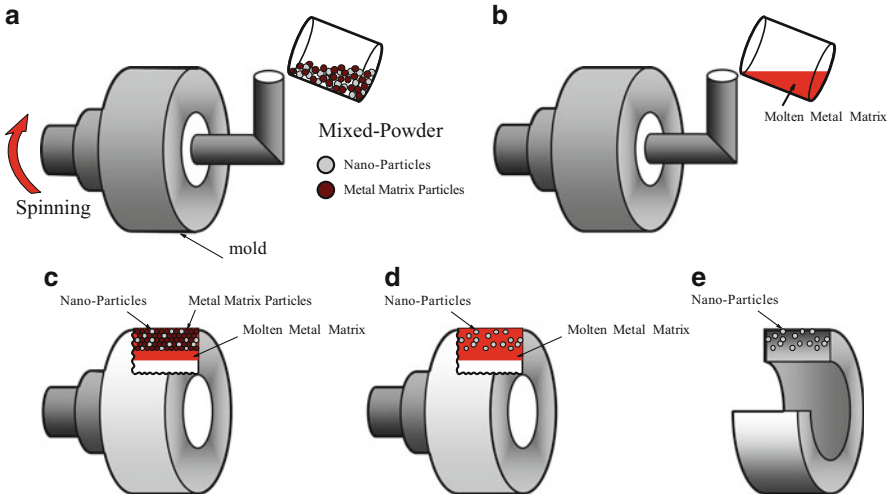

Fig. 9.28 The schematic illustration showing the process of the centrifugal mixed-powder method [40]

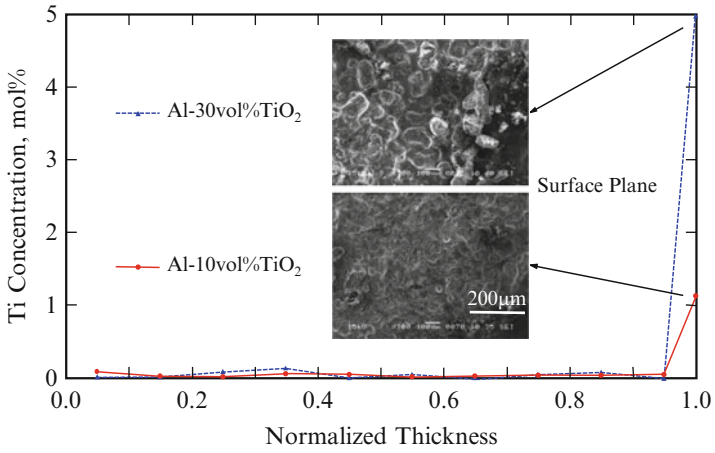

Fig. 9.29 Distributions of Ti concentration in Al–TiO_2 FGMs rings [40]

rings is almost constant from the normalized thickness of 0–0.95, and Ti is not detected inside the Al–TiO_2 FGMs. However, on the surface of the FGMs rings, Ti is detected. It is found that TiO_2 nanoparticles are distributed only on the outer surface of Al–TiO_2 FGMs rings. It is also found that TiO_2 nanoparticle distribution on the surface of the ring may be controlled by the volume fraction of TiO_2 nanoparticle in powder mixture.

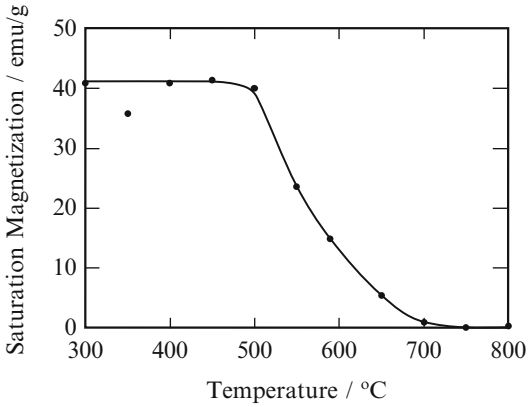

Fig. 9.30 The change in the saturation magnetization with heating temperature. The starting temperature of the reverse transformation, A_s, and the finishing temperature, A_f, are determined to be about 500 °C and 700 °C, respectively

9.6 Magnetic Graded Materials by Inhomogeneous Heat Treatment of SUS304 Stainless Steel

Stainless steel is a major material to produce medical devices due to the superior machinability and corrosion resistance in a biological environment. Development of medical devices, such as stent, catheter, or coil anchor implanted in the human body, has played a key role in the recent progress on medical treatments [41].

Meanwhile, it is well known that plastic deformation of type 304 stainless steel (Fe–18mass%Cr–8mass%Ni) in the austenite (γ) phase can induce formation of the martensite (α′) phase [42]. Martensite and austenite phases are ferromagnetic and paramagnetic at room temperature, respectively. Since the amount of deformation-induced martensite increases with an increase in the local strain, the saturation magnetization of the deformed austenitic stainless steel should also increase with increasing strain. Using this phenomenon, a magnetically graded material can be fabricated by inhomogeneous tensile deformation [43] or inhomogeneous rolling deformation [44] of wedge-shaped 304 austenitic stainless steel specimens. This FGMs fabrication method is termed the martensitic transformation technique.

It is also known that the α′-phase can transform into the γ-phase when the alloy is heated. This reverse transformation is accompanied by a ferromagnetic to paramagnetic transition. Along the temperature gradient from the starting temperature of the reverse transformation to the finishing temperature, the magnitude of saturation magnetization decreases. This phenomenon has also been used to produce a magnetically graded material by inhomogeneous heat treatment of deformed 304 stainless steel [45].

The initial α′-martensite phase in SUS304 stainless steel fiber was introduced by cooling down to the liquid nitrogen temperature (−196 °C). After the cooling, the fiber specimen was annealed within a temperature gradient to introduce the reverse transformation in controlled manner. Figure 9.30 shows the saturation magnetization of heat-treated SUS304 stainless steel fiber plotted as a function of the heating temperature. It is clear that the saturation magnetization decreases with increasing

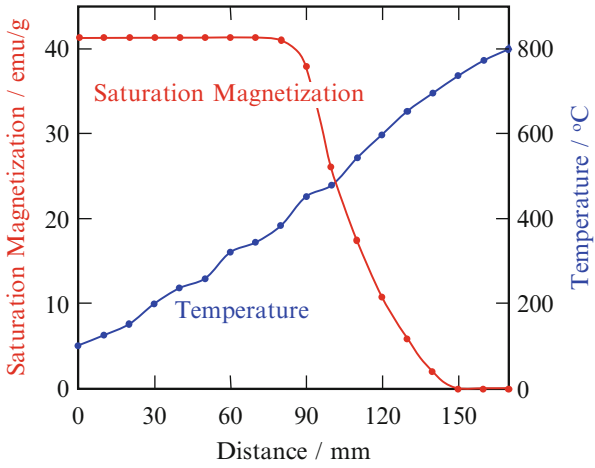

Fig. 9.31 The change of the local temperature of the furnace during the thermal gradient heat treatment of the specimen and the saturation magnetization distribution in the specimen

heating temperature above around 500 °C. This is because the ferromagnetic martensite phase transforms into the paramagnetic γ-austenite phase by the heating process. The saturation magnetization is almost zero in the specimen heated above 700 °C. Therefore, the starting temperature of the reverse transformation, A_s, and the finishing temperature, A_f, are determined to be about 500 °C and 700 °C, respectively.

Figure 9.31 shows the change of the local temperature of the furnace during the thermal gradient heat. Corresponding distribution of the saturation magnetization in the specimen is also shown in Fig. 9.31. As can be seen, the saturation magnetization in the specimen is graded. In this way, a magnetic graded fiber can be successfully fabricated by using the α′ to γ reverse transformation in SUS304 stainless steel.

Magnetically graded SUS304 stainless steel can be used as a magnetic attachment for a dental material. The fabricated material has both magnetic and mechanical gradients. Moreover, it is known that the corrosion resistance of the austenitic phase is better than that of the martensitic phase. Therefore, we can simultaneously fabricate three different gradient properties in one sample.

9.7 Conclusions

In this chapter, the merit of the metallic biomaterials with graded composition and/or microstructure and our recent results, namely, Ti/biodegradable-polymer functionally graded materials (FGMs) for bone tissue fabricated by spark plasma sintering (SPS) method, continuous graded composition in Ti–ZrO_2 bio-FGMs fabricated by mixed-powder pouring method, white ceramic coating on Ti–29Nb–13Ta–4.6Zr (TNTZ) alloy for dental application, Al-based FGMs containing

TiO_2 nanoparticles with antibacterial activity by a centrifugal mixed-powder method, and magnetic graded materials by inhomogeneous heat treatment of SUS304 stainless steel, were described. The materials used for implants need to satisfy the all-round properties of biocompatibility, strength, corrosion resistance, and so on. The concept of FGMs is very useful to satisfy such requirements, and they possess properties within one material, simultaneously.

References

1. Sadollah A, Bahreininejad A (2012) Optimum functionally gradient materials for dental implant using simulated annealing. In: Tsuzuki MSG (ed) Simulated annealing – single and multiple objective problems. InTech, New York, Croatia. doi:10.5772/45640
2. Watari F, Yokoyama A, Matsuo H, Miyao R, Uo M, Kawasaki T, Omori M, Hirai T (2001) Biocompatibility of functionally graded implants. In: Ichikawa K (ed) Functionally graded materials in the 21st century. Kluwer Academic Publishers, Boston, pp 187–190
3. Hirai T (1996) Functional gradient materials. In: Cahan RW, Hassen P, Kramer EJ (eds) Processing of ceramics, Part 2, Materials science and technology, vol 17B. VCH Publishers, Weinheim, pp 293–341
4. Suresh S, Mortensen A (1998) Fundamentals of functionally graded materials, processing and thermomechanical behaviour of graded metals and metal-ceramic composites. IOM Communications Ltd., London
5. Miyamoto Y, Kaysser WA, Rabin BH, Kawasaki A, Ford RG (eds) (1999) Functionally graded materials: design, processing and applications. Kluwer Academic Publishers, Boston
6. Wataria F, Yokoyama A, Omori M, Hirai T, Kondo H, Uo M, Kawasaki T (2004) Biocompatibility of materials and development to functionally graded implant for bio-medical application. Comput Sci Technol 64:893–908
7. Amada S (1995) Hierarchical functionally gradient structures of bamboo, barley, and corn. MRS Bull 20:35–36
8. Watanabe Y, Sato H (2011) Review fabrication of functionally graded materials under a centrifugal force. In: Cuppoletti J (ed) Nanocomposites with unique properties and applications in medicine and industry. InTech, New York, Croatia, pp 133–150
9. Sampath S, Herman H, Shimoda N, Saito T (1995) Thermal spray processing of FGMs. MRS Bull 20:27–31
10. Kondo H, Yokoyama A, Omori M, Ohkubo A, Hirai T, Watari F, Uo M, Kawasaki T (2004) Fabrication of titanium nitride/apatite functionally graded implants by spark plasma sintering. Mater Trans 45:3156–3162
11. Lim Y-M, Park Y-J, Yun Y-H, Hwang K-S (2002) Functionally graded Ti/HAP coatings on Ti–6Al–4 V obtained by chemical solution deposition. Ceram Int 28:37–41
12. Yin GF, Luo JM, Zheng CQ, Tong HH, Huo YF, Mu LL (1999) Preparation of DLC gradient biomaterials by means of plasma source ion implant-ion beam enhanced deposition. Thin Solid Films 345:67–70
13. Sato M, Tu R, Goto T, Ueda K, Narushima T (2009) Preparation of functionally graded Bioceramic film by MOCVD. Mater Sci Forum 631–632:193–198
14. Watanabe Y, Iwasa Y, Sato H, Teramoto A, Abe K, Miura-Fujiwara E (2011) Microstructures and mechanical properties of titanium / biodegradable-polymer FGMs for bone tissue fabricated by spark plasma sintering method. J Mater Process Technol 211:1919–1926
15. Reilly DT, Burstein AH (1975) The elastic and ultimate properties of compact bone tissue. J Biomech 8:393–396
16. Narushima T (2005) Titanium and its alloys as biomaterials. J Jpn Inst Light Met 55:561–565

17. Ueda M, Sasaki Y, Ikeda M, Ogawa M (2009) Chemical-hydrothermal synthesis of bioinert ZrO_2-TiO_2 film on Ti substrates. Mater Trans 50:2104–2107
18. Tsuji H, Tezuka Y, Saha SK, Suzuki M, Itsuno S (2005) Spherulite growth of L-lactide copolymers: effects of tacticity and comonomers. Polymer 46:4917–4927
19. Sato H, Umaoka S-i, Watanabe Y, Kim I-S, Kawahara M, Tokita M (2007) Biodegradable fiber reinforced Ti composite fabricated by spark plasma sintering method. Mater Sci Forum 539–543:3201–3206
20. Miura-Fujiwara E, Teramoto T, Sato H, Kobayashi E, Watanabe Y (2010) Fabrication of Ti-based biodegradable material composites prepared by spark plasma sintering method. Mater Sci Forum 654–656:2158–2161
21. Hasebe T, Kobayashi E, Tezuka H, Sato T (2013) Effects of sintering conditions on mechanical properties of biomedical porous Ti produced by spark plasma sintering. Jpn J Appl Phys 52:01AE03 (4 pages)
22. Wen CE, Mabuchi M, Yamada Y, Shimojima K, Chino Y, Asahina T (2001) Processing of biocompatible porous Ti and Mg. Scr Mater 45:1147–1153
23. Watanabe Y, Miura-Fujiwara E, Sato H (2010) Fabrication of functionally graded materials by centrifugal slurry-pouring method and centrifugal mixed-powder method. J Jpn Soc Powder Powder Metall 57:321–326
24. Kang CG, Rohatgi PK (1996) Transient thermal analysis of solidification in a centrifugal casting for composite materials containing particle segregation. Metall Mater Trans B 27:277–285
25. Watanabe Y, Yamanaka N, Fukui Y (1998) Control of composition gradient in a metal-ceramic functionally graded material manufactured by the centrifugal method. Compos Part A 29A:595–601
26. Piconi C, Maccauro G (1999) Review Zirconia as a ceramic biomaterial. Biogeosciences 20:1–25
27. Watanabe Y, Miura-Fujiwara E, Sato H (2011) Fabrication of functionally graded materials by combination of centrifugal force and sintering method. J Jpn Soc Powder Powder Metall 58:11–17
28. Jayachandran M, Tsukamoto H, Sato H, Watanabe Y (2013) Formation behavior of continuous graded composition in Ti-ZrO_2 functionally graded material fabricated by mixed-powder pouring method. J Nanomater 2013:504631 (8 pages)
29. Miura E, Tabaru T, Liu J, Tanaka Y, Shiraishi T, Hisatsune K (2004) Effect of gold coating on interfacial reaction between dental porcelain and titanium. Mater Trans 45:3044–3049
30. Kuroda D, Niinomi M, Morinaga M, Kato Y, Yashiro T (1998) Design and mechanical properties of New β type titanium alloys for implant materials. Mater Sci Eng A243:244–249
31. Niinomi M, Hattori T, Morikawa K, Kasuga T, Suzuki A, Fukui H, Niwa S (2002) Development of low rigidity β-type titanium alloy for biomedical applications. Mater Trans 43:2970–2977
32. Miura-Fujiwara E, Yamada S, Obata A, Sato H, Watanabe Y, Kasuga T, Niinomi M (2012) Oxidation behavior and effect of layer thickness on whiteness and exfoliation behavior of Oxide Film Formed on Ti-Nb-Ta-Zr Alloy. In: Proceedings of the Ti-2011 conference, III, China National Convention Center, Beijing, China, pp 2116–2120
33. Miura-Fujiwara E, Mizushima K, Yamada S, Watanabe Y, Kasuga T, Niinomi M, Yamasaki T (2013) Aesthetic and mechanical properties of oxide coated Ti-Nb-Ta-Zr alloys as a dental material. In: Proceedings of the 8th pacific rim international conference on advanced materials and processing, TMS (The Minerals, Metals & Materials Society), Hilton Waikoloa Village, Waikoloa, HI, USA, pp 1543–1550
34. Obata A, Miura-Fujiwara E, Shimizu A, Maeda H, Nakai M, Watanabe Y, Niinomi M, Kasuga T (2013) White-ceramic conversion on Ti-29Nb-13Ta-4.6Zr surface for dental applications. Adv Mater Sci Eng 2013:501621 (9 pages)

35. Miura-Fujiwara E, Mizushima K, Watanabe Y, Kasuga T, Niinomi M (2014) Color tone and interfacial microstructure of white oxide layer on CP Ti and Ti-Nb-Ta-Zr alloys. Jpn J Appl Phys 53:11RD02
36. Hasegawa A, Motonomi A, Ikeda I, Kawaguchi S (2000) Color of natural tooth crown in Japanese people. Color Res Appl 25:43–48
37. Shiba W, Uno M, Ishigami H, Kurachi M (2009) Means for reproducing shade guide color with laboratory-cured prosthetic composite. J Gifu Dent Soc 35:149–159
38. Yuan W, Ji J, Fu J, Shen J (2008) A facile method to construct hybrid multilayered films as a strong and multifunctional antibacterial coating. J Biomed Mater Res Part B 85B:556–563
39. Tang W, Chen Z, Katoh S (2004) Preparation of a nanocrystalline TiO_2 photocatalyst using a dry-process with acetylene black. Chem Lett 33:1200–1201
40. Watanabe Y, Inaguma Y, Sato H, Miura-Fujiwara E (2009) A novel fabrication method for functionally graded materials under centrifugal force: the centrifugal mixed-powder method. Materials 2:2510–2525
41. Uenishi K, Seki M, Takatsugu M, Kunimasa T, Kobayashi KF, Ikeda T, Tsuboi A (2002) Microstructure and tensile strength of stainless steel wires micro spot melted by YAG laser. Mater Trans 43:3083–3087
42. Mangonon PL, Thomas G (1970) Structure and properties of thermal-mechanically treated 304 stainless steel. Metall Trans 1:1587–1594
43. Watanabe Y, Nakamura Y, Fukui Y, Nakanishi K (1993) A magnetic-functionally graded material manufactured with deformation-induced martensitic transformation. J Mater Sci Lett 12:326–328
44. Watanabe Y, Kang SH, Chan JW, Morris JW Jr (1999) Fabrication of magnetically graded material by rolling deformation of wedge-shaped 304 stainless steel. Mater Trans JIM 40:961–966
45. Watanabe Y, Momose I (2004) Magnetically graded materials fabricated by inhomogeneous heat treatment of deformed stainless steel. Ironmak Steelmak 31:265–268